
On the Extraction of Microseismic Ground Motion from Analog Seismograms for the Validation of Ocean-Climate Models

Lecocq Thomas ^{1,*}, Arduin Fabrice ², Collin Fabienne ¹, Camelbeeck Thierry ¹

¹ Seismology–Gravimetry, Royal Observatory of Belgium, Brussels, Belgium

² University of Brest, CNRS, IRD, Ifremer, Laboratoire d’Océanographie Physique et Spatiale (LOPS), IUEM, Brest, France

* Corresponding author : Thomas Lecocq, email address : thomas.lecocq@seismology.be

Abstract :

We report on a pilot demonstration of the usefulness of analog seismograms to improve the database of ocean storms before the 1980s by providing additional data for the quantitative validation of ocean wave modeling, in particular for extreme events. We present a method for automatic digitization of paper seismograms to extract microseismic ground-motion periods and amplitudes. Each minute of the original paper records is scanned and vectorized. The amplitudes are calibrated based on the original metadata taken from official bulletins. The digitized time series is processed to extract power spectral densities, which are compared with modeled microseisms levels computed using a numerical ocean wave model. As a case study, we focus on one month of data recorded at the Royal Observatory of Belgium (ROB) from January to February 1953, around the “Big Flood” event, a tragic storm surge that flooded the lowlands of England, the Netherlands, and Belgium on 1 February 1953. The reconstructed spectrograms for the three components of ground motion show clear storm signatures that we relate to specific sources in the North Atlantic Ocean. However, our models of the Big Flood event based on these data do not result in the expected amplitudes as modeled compared to the observational data when the storm reached its maximum in the southern North Sea. We suggest that the source of microseisms recorded at ROB is related to the primary microseism generated in the North Sea, at periods of 7–8 s. Other discrepancies identified suggest small modifications of the source locations or energy. Reconstructed horizontal and vertical ground motions are coherent. This is a good news for the purpose of present-day analyses of constructing twentieth century ocean-climate models, especially as during much of that time only horizontal seismographs were installed at observatories.

29 Introduction

30 Seismologists observed and recorded the Earth's continuous ground motions long before the onset of
31 digital seismography, as early as 1855 (Shearer, 2019). At some locations, analog seismic data were
32 recorded on smoked paper, with ink (e.g. drum recorded), or on photographic paper into the 1980s.
33 For ocean waves, visual observations from ships make up nearly all the available data until 1946 with
34 only a few instrumented records, which only became more common in the 1980s with the deployment
35 of buoys (e.g. Gilhousen, 1987; Meindl and Hamilton, 1992). Global measurements of major ocean
36 storms using wave heights became ubiquitous as of 1993 with satellite measurements Davis (2007), but
37 coverage is usually not sufficient to record the peak of storms, and our general knowledge of the ocean
38 wave climate therefore heavily relies on numerical models based on wind parameters obtained from
39 atmospheric reanalyses (Raschle and Arduin, 2013; Reguero et al., 2019). Because the wind speed and
40 direction at sea level are diagnostic variables with few measurements before 1994, these estimates and
41 their climatic trends are prone to artificial biases.

42 Another source of quantitative data comes from the microseisms recorded by seismometers (Bernard,
43 1990). Microseisms have been extensively studied since the early days of seismology (for a review
44 see Ebeling, 2012, and references therein) mostly because of their presence in *all* seismic records. A
45 microseism is defined as continuous ground motion arising from the interaction between the atmosphere,
46 the oceans and the solid Earth through energy transfer via the water column (for a complete review
47 see Nakata et al., 2019, and references therein). Seismic records have been used to study the regional
48 distribution of microseism sources for example, by Donn and Blaik (1952) who used a simple tripartite
49 azimuth computation to study the 1950 storm season in the Northern Atlantic, or by Friedrich et al.
50 (1998) using the first digital records of the Gräfenberg Array, Germany (Harjes and Seidl, 1978) to
51 locate multiple sources of microseisms in the North Atlantic ocean. Seismic data was also compiled by
52 Aster et al. (2008, 2010) for studying the long term evolution of microseism power based on all available
53 digital data from the Seismic Research Observatory, the High-Gain Long Period and Global Seismic
54 Network (Albuquerque Seismological Laboratory (ASL)/USGS, 1972, 1974, 1988).

55 Using 40 years of seismic records (1954-1998) from Hamburg, Germany, Grevemeyer et al. (2000)

56 showed that measurements on historical seismic records are related to possible changes in the wave
57 climate in the northeast Atlantic Ocean. Similarly, Dahm et al. (2005) used historical seismic data
58 from different locations in Europe and showed a good correlation between them for specific storm
59 periods. Recently, Gualtieri et al. (2018) showed that tropical cyclones can be tracked using the spectral
60 content of the microseisms generated by them, and that their intensity can be derived from the spectral
61 amplitude of the short period secondary microseism. Hanafin et al. (2012) showed that very long-period
62 microseisms (above 9 s) are proportional to long ocean wave periods (twice the seismic period, over 18 s)
63 and considered them to be finger prints of extreme ocean storms.

64 The magnitude of microseisms is not simply related to the height of ocean waves (Obrebski et al.,
65 2012, e.g.), it is therefore necessary to transform a modeled wave climate into microseismic amplitudes
66 as applied by Stutzmann et al. (2012) to validate a global microseismic model. Stopa et al. (2019)
67 utilized a similar model for improving wave hindcasts by modifying the wind field in time and space,
68 transforming wind to waves, and waves to microseisms that can be compared with seismic records. Here
69 we propose a new seismic digitization method, processing scanned paper seismograms from the analog
70 instrumental epoch to extract microseism amplitude and frequency content (spectra). Those spectra,
71 properly referenced in time and amplitude, are then compared with a microseism generation model
72 based on the WAVEWATCH III wave model (Tolman and the WAVEWATCH III Development Group,
73 2014). For this pilot project, we will focus on the "Big Flood" of 1953, a massive storm surge event that
74 dramatically flooded low-lands of the Netherlands, Belgium and England and caused 2165 fatalities.

75 **Seismic analog records**

76 The first seismic records made at the Uccle station (UCC) of the Royal Observatory of Belgium date
77 back to 1898 (Royal Observatory of Belgium, 1985; Van Camp and Camelbeeck, 2004) and were acquired
78 using a von Rebeur-Ehlertr triple horizontal pendulum built by Bosch (Strasbourg, France). At the
79 beginning of the 20th century, the ROB owned two Wiechert seismometers: one 1000 kg horizontal
80 (installed in 1910, decommissioned in the 1970's) and one 1300 kg vertical (1911-1970's) seismometer,
81 two Galitzin double-pendulum horizontal seismometers (1911-1914 and 1919-1962) and one Galitzin-

82 Wilip vertical seismometer (1930-1970's). This Galitzin-Wilip seismometer was difficult to stabilise and
83 its records were unreliable, making it essentially useless between 1930 and 1935 (Somville, 1930, 1931,
84 1932, 1933, 1934, 1935) until it was heavily modified by Somville in 1936 (Somville, 1936, 1937a,b) to be
85 stable at different periods while ensuring that damping and recording remained identical to the original
86 Galitzin-Wilip. Because of its modifications, we call this new instrument the Galitzin-Wilip-Somville
87 seismometer.

88 The Wiechert seismometers used a pen to scratch rolls of smoked paper as recorder, while Galitzin
89 seismometers used a galvanometric system to direct a beam of light onto photographic paper. The
90 advantage of the photo records over smoked paper is that the photo records generally have greater
91 contrast between the trace and the background, which could be greyish or scratched on smoked paper.
92 The friction of the pen on paper also altered the quality of the records, although this effect was more
93 important for large amplitude resulting from seismic events than for microseisms.

94 The timing of seismic records is, by nature, critical. The recording systems at the ROB were
95 synchronised with the "Bureau de l'Heure" (the "Time Office") operated by the ROB in a close-by
96 building. The timing accuracy was 1 second in 1909 and 0.1 second as of 1913 (Somville, 1914, pp 176).
97 The reference clocks, named "fundamentals", were 4 Rieffler pendulums installed in a temperature-
98 controlled basement until 1955 when the first quartz clocks were installed. The relative time encoding
99 on paper seismograms is generally done by one of the three following ways: (1) a gap of one or more
100 seconds at the end of each minute, generated by lifting the needle off the smoked paper or by intercepting
101 the light beam to photographic paper; (2) a spike or (3) a translation of a few millimetres of the trace.
102 Our Galitzin records are of type (1): the photographic records show one second gaps at the end of every
103 minute. The absolute time encoding is done by interrupting the light beam for 1 second every hour,
104 allowing to measure the time correction to add to the beginning of every minute.

105 The ROB still owns most of the analog records, either in paper form stored in one single wooden box
106 per year of data, or digitized on microfilm (which records could also be scanned in the future, depending
107 on the quality of preservation).

108 **Digitizing paper seismograms and extracting ground motion**

109 Extracting digital seismic traces from scans (images) has been the subject of numerous articles in the
110 past 20 years and the digitizing process can be classified either manually by clicking on all the wiggles
111 of a seismic trace (e.g. Bromirski and Chuang, 2003; Pintore et al., 2005), or automatically using image
112 processing techniques to extract the wiggles (e.g. Baskoutas et al., 2000; Church et al., 2013; Wang
113 et al., 2014). Bromirski and Chuang (2003) show an example on their website ([http://iodlabs.ucsd.](http://iodlabs.ucsd.edu/peter/seismology/SeisDig.html)
114 [edu/peter/seismology/SeisDig.html](http://iodlabs.ucsd.edu/peter/seismology/SeisDig.html), last accessed September 2019) of scanned seismograms from a
115 Galitzin-Wilip vertical seismometer for January 1941 and highlight its similarity with spectrograms that
116 can be obtained nowadays with modern digital seismic data. The semi-Automatic DigitSeis digitization
117 software (Bogiatzis and Ishii, 2016) includes the automatic detection and digitization of seismic traces
118 and timing marks while allowing manual corrections and adjustments from the user.

119 Our method is comparable to the one described in Wang et al. (2014) and is comprised of the
120 following steps, with changes to the methodology as developed in this study marked with a *: Scan, Color
121 Inversion, Thresholding*, Binarization, Rotation*, Region "Labelling"*, Line Thinning - Skeletonization
122 and ObsPy Trace Object Creation*. These steps are described in the following section. The digitization
123 algorithm is written in Python and makes use of state of the art Python modules, and is available as
124 Jupyter Notebooks (see Data & Resources).

125 **Scanning paper seismograms**

126 The scanning of paper seismograms is time-consuming and tedious, but essential for the conservation of
127 our archives (Okal, 2015). Until recently, ROB scans were restricted to significant event records. For this
128 study, seismograms were scanned using a Contex HD Ultra scanner capable of ingesting a 841 mm-wide
129 sheet of paper (width of an A0 ISO 216 standard). Such a scanner supports scanning photographic
130 paper, but not smoked paper due to potential damage from the scanner drive rollers. The final image is
131 saved to TIFF file format. For consistency, we used naming conventions with station name (e.g. UCC),
132 seismometer orientation ('v', 'n-s' or 'e-w'), and the date of the record. For processing microseisms
133 records, a resolution of 300 dpi is sufficient and is less computationally expensive during the processing

134 than 1200 dpi, i.e., the maximal resolution of the scanner.

135 **Color inversion, thresholding, binarization and rotation**

136 Smoked paper seismograms have a black background (the smoke) and whitish traces, scratched by the
137 pen, while developed photographic papers have a white background and a black trace. In order to easily
138 identify both kind of traces using the same algorithm, the photographic images are photo-inverted to
139 obtain white traces. A threshold (Otsu, 1979) is applied to the image in order to reject small under-
140 represented tones from the image. Lastly, the image is binarized, i.e. all positive values (traces) are set
141 to 1 and the background to 0.

142 Next, we rotate the image to adjust for slight misalignment of the sheet in the scanner. This step
143 is done using a Hough Transform (Hough, 1962; Duda and Hart, 1972), i.e. a computer visualization
144 technique to automatically identify straight lines in an image. We only compute the transform for angles
145 in a $\pm 5^\circ$ range. The technique outputs identified lines, described by their location and angle. The
146 image is then rotated by the median angle to horizontalize the traces.

147 **Region labelling and skeletonization**

148 The "labelling" operation consists of identifying regions of the image that are connected and form a
149 shape, in our case, continuous chunks of seismic traces. The regions have (x,y) coordinates in the image
150 space and can therefore be located and easily manipulated for further processing. This processing will
151 only occur if the region identified is long and narrow, as we expect short and wide regions to contain
152 bad data, glitches, handwriting or other irrelevant information. The current version of the computer
153 code developed here only works with non-overlapping traces. This means that strong teleseismic events
154 or calibration pulses will be ignored and skipped. Computer vision and machine learning techniques
155 should be exploited in the future to overcome this limitation.

156 A process of line thinning is then required in order to reduce a two-dimensional region of an image
157 containing an object of random shape to a simple line. 2D objects can be defined by their "skeleton",
158 or "central line". In the case of seismic records, this skeleton will be centered in the white pixels of the

159 trace. Once identified, each trace is stored together with its (x,y) coordinates on the image.

160 **ObsPy Trace creation**

161 The identified seismic traces are analyzed using standard modern processing, carried out by creating
 162 one ObsPy Trace object per trace. The (x,y) coordinates of the traces are used to sort them time wise
 163 and the length of each trace is 59 seconds. To evaluate the sampling rate of each trace, we consider
 164 the median length of all traces identified on one sheet and compute the number of pixels per second
 165 (pps), which is the sampling rate. On most of our scans at 300 dpi, the trace length is 359 pixels, or
 166 around 6.085 Hz. This corresponds to a movement of the light beam on the paper of 3 cm per minute.
 167 All traces are then linearly detrended, resampled (interpolated) to a common 8 Hz sampling rate using
 168 a Lanczos interpolation, tapered with a 0.5 s taper on both ends and highpass-filtered above 0.08 Hz
 169 (12.5 s). The start time of each trace is computed from its (x,y) coordinates.

170 **Instrument response correction**

171 The functioning and the instrument response of the Galitzin seismometers are known and documented
 172 in the official Bulletins of the ROB (Somville, 1922a,b). Table 1 shows the parameters for the Galitzin
 173 seismometers as they were operated in 1953 (Somville, 1953). The calibration values for the transfer
 174 factor k are trusted for the horizontal unmodified pendulums. For for the vertical, heavily modified
 175 instrument, we didn't find any explanation on its determination but only its value in the reports from
 176 Somville (1937b). This vertical instrument has never been used to calculate the ground motion amplitude
 177 (mentioned in the Bulletins) until it was decommissioned.

178 Using Table 1 and Galitzin's formulations (Galitzin, 1911, pp 107-108), we can recompute the real
 179 ground motion (x_m) from the measured amplitudes on the paper (y_m), i.e. amplitude instrumental
 180 response for different periods (T_p):

$$x_m = C_1(1 + u_1^2)(1 + u^2)\sqrt{1 - \mu^2 f(u)}\frac{y_m}{T_p} \quad (1)$$

181 with $C_1 = \frac{\pi l}{kA_1}$, $f(u) = \left[\frac{2u}{1+u^2}\right]^2$, and $u = \frac{T_p}{T}$, $u_1 = \frac{T_p}{T_1}$

182 where T is the period of the pendulum, T_1 the period of the galvanometer, l the reduced pendulum
183 length, μ the damping constant, A_1 the distance of the drum from the galvanometer mirror and k the
184 transfer factor (Galitzin, 1911, p. 103). This step evidenced that the k transfer factor for Galitzin-
185 Willip-Somville seismometer was not correct, because digitized seismic traces are systematically three
186 times larger than on the horizontal components. It is expected that the amplitude of the ground motions
187 from Rayleigh and Love waves should have a ratio of horizontal to vertical $H/V \approx 1.0$ (Darbyshire, 1954;
188 Juretzek and Hadziioannou, 2016). We therefore empirically determined the k factor to one third of its
189 value to scale the vertical traces to the trusted horizontal ones.

190 The amplitude response of the Galitzin seismometers (Figure 1) can be utilized for studying mi-
191 croseisms because they have a maximal sensitivity in the primary (secondary) microseism band for the
192 horizontal (vertical) Galitzin, respectively.

193 Since the very beginning of their usage, Galitzin seismometers were subject to criticisms about the
194 non-validity of the assumption that the recorded data precisely reproduced the ground displacement
195 (McComb and Wenner, 1936; Wenner and McComb, 1936). Because the eigenperiods of the Galitzin
196 seismometer and galvanometer are the same, a slight phase difference between the true and recorded
197 ground motions is incurred when the period of the recorded ground motion differs from the nominal
198 seismometer period. The negative assessment was confirmed and there is indeed a difference in phase
199 between the two when the period of the recorded waves are larger or smaller than the nominal frequency.
200 This discrepancy was also verified by Somville for the Galitzin-Willip vertical seismometer owned by
201 the ROB. The phase shifts observed are orders of magnitude smaller than the studied period (0.1 s
202 shift or less at 1.0 s). This instrumental shortcoming could have a strong impact on phase arrival
203 time measurements, but is negligible for the study of microseism periods and amplitudes averaged over
204 minutes to hours.

205 The dominant period of each one minute trace is extracted from its power spectral density (PSD,
206 see below) and is used in Equation 1 to obtain the amplification factor, i.e. removing the instrument's
207 amplitude response. The Galitzin seismometers and the digitizing technique have very little sensitivity
208 to frequencies above 1 Hz.

Power Spectral Density

The PSD of each seismic trace is computed using Welch's method (Welch, 1967). This method is known to reduce noise in the power spectra at the expense of reducing the frequency resolution because of frequency binning, which is efficient for obtaining information on the broad secondary microseismic peak.

The Welch method proceeds by splitting the signal in overlapping segments that are then windowed, in our case with a Hanning Window (Blackman and Tukey, 1958), which more heavily weights the data at the center of the window. The windowed segments are then converted to a periodogram using the squared magnitude of the discrete Fourier Transform. The resulting periodograms are averaged to reduce the variance of the power measurements.

The final product of our processing are three-hour medians of the individual, minute-long PSDs. This granularity was chosen to match the one used in the ocean modeling.

Ocean microseism generation modeling

Our microseism model is a combination of a numerical wave model and a transformation of wave spectra into microseisms. The wave model is described in Rascle and Ardhuin (2013) and covers the world ocean, with a spatial resolution of 0.5 degree in longitude and latitude. The choice of parameterizations for the wind-wave generation and dissipation is particularly important for the directional distribution of the wave energy and the resulting strength of microseism sources (Ardhuin et al., 2011). It is forced by winds from the ECMWF (European Centre for Medium-Range Weather Forecasts) 20th century reanalysis (Poli et al., 2016). Based on satellite-derived wave heights for the year 2001, the wind-wave coupling coefficient β_{\max} was set to 1.7, giving a good representation of even the extreme wave heights (Stopa et al., 2019). The wave model was run with and without shoreline reflection coefficient R for the wave energy.

The transformation of wave spectra to microseisms follows Ardhuin et al. (2011), with a summation of microseism sources (Figure 4) along great circle paths and an attenuation with a constant Q coefficient.

234 For UCC, we have used $Q = 200$ or $Q = 300$ and $R = 0.1$. The Q values limit the range of the best
235 fit obtained by (Stopa et al., 2019) for seismic stations in continental Europe (180 for station ESK
236 (Scotland), 220 for GRA (Germany) or 230 for SSB (France)). The $R = 0.1$ is larger than traditionally
237 used but our objective here is to show first order comparison and not to invert for R . Yet, for the
238 years 2001 to 2014, these constant coefficients typically give a correlation coefficient $r = 0.95$ between
239 the measured vertical ground displacement standard deviation over 3 hours and the modeled value of
240 the same parameter, meaning that it is highly probable that the modeled events correspond to the
241 synchronous ones observed at UCC. This processing predicts ground motions in a period/frequency
242 band comparable to the band in which the Galitzin seismometer sensitivity is the greatest. Arduin
243 et al. (2011) estimated that strong sources located at 1000 km away over a uniform $100 \times 100 \text{ km}^2$ area
244 would induce a displacement variance of $1 \mu\text{m}^2$ when neglecting attenuation and seismic energy loss.
245 Considering attenuation and ocean-solid earth coupling, the UCC station has its largest sensitivity in the
246 first 1000 km around it and is sensitive to strong sources occurring up to 2000 km (Figure 2). Looking at
247 the spatial distribution of the modeled sources, we thus expect the UCC station to be sensitive to storms
248 in the deep waters off the British isles, the Norwegian coast, south of Iceland along the mid-Atlantic
249 ridge and the north-western Mediterranean sea.

250 **Microseismic activity in January-February 1953**

251 At the end of January 1953, a storm formed in the North Atlantic ocean (Figure 2) and moved towards
252 the northern tip of Scotland before changing direction to the south-east, in the North Sea towards the
253 southern part of Denmark (Wemelsfelder, 1953; Wolf and Flather, 2005). While moving south-east
254 in the North Sea, although its low-pressure center was not exceptionally deep, this storm generated
255 strong winds and, combined with high spring tides, higher-than-usual sustained surge. During the night
256 from 31 January to 1 February 1953, the surge height was maximal in the low-lands of England, The
257 Netherlands and Belgium. Extreme flooding due to dike failures led to a disastrous number of fatalities:
258 1836 in the Netherlands, 307 in the United Kingdom and 22 in Belgium (Gerritsen, 2005). In the
259 Netherlands, a total of 200000 ha were flooded, 100000 people were evacuated, 47300 houses damaged

260 from which 9215 badly or irreparably (Wemelsfelder, 1953). This disaster, called "The Big Flood", was
261 at the impetus for the creation of the Delta Plan that today protects the Dutch lowlands from future
262 surges (Wemelsfelder, 1953). In Belgium, between 1953 and 1977, more than 3.7 billion Belgian Francs
263 (40 BEF = 1 EUR ; 92 million euros in 1977 euros or, if corrected for inflation, 312 million euros in 2019
264 euros) were invested to repair and secure dikes and rivers within the Sigma Plan (Ministère des Travaux
265 Publics, 1977). For this case study, we therefore decided to scan the records of the three components of
266 the Galitzin seismometer between 15 January and 15 February 1953, centered on the "The Big Flood"
267 event and compare them to the modelled ground motion.

268 Despite a few records being incomplete or missing (sadly, the one containing the 1 February when
269 the storm surge was maximal), the ground motion induced by this storm can still be extracted and
270 PSDs reconstructed. One explanation for the absence of the records during the maximum of the storm
271 is that the developed paper was unusable due to bad, probably clipped off-scale records. This hypothesis
272 is supported by the records from the horizontal components, which exhibit an extreme amplification
273 of the traces on the mornings of 31 January and 2 February. Ninety analog seismograms (1 month, 3
274 components) were systematically processed using the work flow as described above and provided the
275 amplitude and the dominant period of each minute, together with the 3-hour Power Spectral Densities
276 of the ground motion recorded at UCC. Figure 3 shows the time evolution of the Power Spectral Density
277 - or spectrogram - of the microseisms records and of the model generated for the same period. There are
278 five periods of significant microseismic activity seemingly higher than a background level that could be
279 estimated at $0.25 \mu m$: 17-21 January, 26-30 January, 31 January - 2 February, 4-5 February and finally
280 8-12 February.

281 Discussion

282 The microseismic activity recorded by the Galitzin and Galitzin-Wilip-Somville seismometers at station
283 UCC shows strong changes during January-February 1953 (Figure 3). The spectrograms for the three
284 components are coherent and we can therefore average the three spectrograms and take advantage of
285 their slightly different time coverage/gaps. To compare the spectrograms with the modeled ground

286 motion, we extract time series of the total amplitude of the ground motion (displacement, δ_{RMS}) and of
287 the dominant period of the seismic waves from the observed and the modeled data (Figure 5). Spectra
288 (Figure 3) are processed as in Arduin et al. (2011). The δ_{RMS} of the microseisms is defined as the
289 square root of the integral of the microseisms spectrum:

$$290 \quad \delta_{RMS} = \sqrt{\int_{0.08Hz}^{0.32Hz} F_{\delta} df_s}$$

291 with F_{δ} being the power spectrum of the ground displacement and f_s the period of the seismic wave.

292 There is good agreement between the ground motion amplitudes and dominant periods, except for
293 the 17-21 January and the Big Flood event (24 January - 2 February). Because of the original granularity
294 of our data set, we also make use of the individual maximum ground motion per minute and compute
295 their mean, median and standard deviation values per 3 hours (Figure 5). In the following, we discuss
296 the different events of interest with respect to the modeled microseisms sources (Figure 4).

297 The microseism source models do not reproduce the 17-21 January event (E1 on Figures 3, 4 and 5).
298 The model (Figure 4) locates sources close to the Azores, distributed sources between the Azores and the
299 southern tip of Greenland and, at the same time, strong localized sources on the Norwegian coast and
300 around the Shetland Islands. During this period, very strong sources are also located at the southern
301 tip of Greenland. Changes of Q are not sufficient to significantly increase the effect of this storm, so we
302 suggest that the two broad sources should have been more energetic than currently modeled.

303 For the 24-25 January event visible on the modeled data, there is a slight increase in amplitude, but
304 the maximum is missed and could not be investigated due to a gap in the data.

305 The 26-30 January interval (E2) corresponds to sources illuminating the entire West coast of Europe,
306 including south Iceland, the U.K. and Ireland, together with a broad source in the Norwegian Sea (Figure
307 4). The model predicts reduced ground motion amplitudes with less variations than in the observed
308 data. The strongest peak in the observed data corresponds to the arrival of the modeled seismic sources
309 on the west coast of the U.K. and Ireland.

310 The Big Flood, the 31 January - 2 February storm (E3) shows the largest discrepancy between the
311 model and observations. During this period, the storm moved around the northern tip of Scotland and
312 then progressed southwards towards the English Channel. The highest peak in microseism amplitude

313 and longest-period microseisms are completely absent in the modeling. The difference between observed
314 and predicted values is almost twofold ($1 \mu\text{m}$) in amplitude and 1 s in period. The southern North
315 Sea is characterized by shallow waters (10 to 150 m) with weak coupling between ocean waves and
316 the ground and therefore should contribute only low amplitude microseisms, which is what the model
317 indeed predicts. The data, however, indicates that strong microseismic energy was recorded at the
318 time of the storm. To resolve this discrepancy, we increased the Q factor from 300 to 400 for the
319 area because we know from other seismic studies (Camelbeeck, 1985; El Bouch et al., 2002; Van Noten
320 et al., 2017; Mayor et al., 2018) that the attenuation in northeast Belgium is low due to the presence
321 of the WNW-ESE extending Brabant-London Massif, but the changes are too subtle to account for the
322 nearly doubled amplitude difference. Another explanation could be that the modeled data represents
323 secondary microseisms, as there is recent evidence that short period (5 - 8 s) primary microseisms could
324 be generated in the North Sea (Becker et al., 2019). This duality of generated microseisms would explain
325 the strong energy measured, as well as the dominant period around 7-8 s, coherent with the work of
326 Choi et al. (2018) who calculated the dominant sea wave periods to be between 7 and 9 s during the
327 maximum of the storm. The study of primary microseism generation, specifically in the North Sea, has
328 recently been addressed (Juretzek and Hadziioannou, 2017; Becker et al., 2019) and should soon provide
329 new modeling theories to compare with our results. The local wind field around UCC, also known as
330 a source of seismic noise, for example, by its interaction with trees, can be ruled out, as most of the
331 seismic energy radiated is at the first mode of resonance of trees, around a 1 to 5 s maximum (Roux
332 et al., 2018), while higher modes occur at much higher frequency.

333 The trends in recovered UCC microseism frequency content and amplitudes during the 4-5 February
334 period (E4) are consistent with sources located in the center of the North Atlantic. The modeled
335 amplitudes are slightly higher than the observations but the trends are similar. To match those, either
336 Q should be lower (more attenuation) or the source should be further away or weaker.

337 The trends during the 8-12 February interval (E5) are consistent with to sources located south of
338 Iceland, moving south towards the west coasts of the U.K. and Ireland, then Brittany (France), Bay
339 of Biscay (northeast Atlantic Ocean), Galicia (Spain) and the entire west coast of Spain and Portugal,

340 ending with sources located on the west coast of Sardinia. The model exhibits similar amplitudes as the
341 data, but with a +1 day lag with respect to the maximum of the 8-12 February storm. The maximum
342 observed amplitudes occurred on 10 February, when the storm hit Scotland simultaneously with Galicia
343 and the Bay of Biscay. There could also be parts of the southern North Sea affected by stronger waves,
344 and the explanation of the absence of the primary microseism above could also apply here.

345 Differences between observed and modelled ground motion could also arise from the uncertainties
346 on the calibration parameters of the instruments. The response of horizontal Galitzin pendulums have
347 been known and used during most of the century and are trusted. An error in the amplification factor
348 would lead to a scalar multiplication factor between observed and modelled time series. An error in the
349 shape of the amplitude-frequency response could explain differences, but our results show that periods
350 of activity having the same dominant period exhibit different behaviours in terms of recovered ground
351 motion (E1 versus E4, for example).

352 Conclusions

353 The digitization of analog seismograms allows reconstructing the evolution of the microseismic energy
354 recorded at a single location. Because of its importance for locating earthquakes, the timing of the
355 seismic records has always been the subject of great attention and is very accurate in Uccle since 1913,
356 which allows obtaining a high time resolution of observations. For each minute of digitized data, we
357 are able to produce one Power Spectra Density spectrum. Averaging them by hour or 3 hours, we
358 can compare the seismic energy observations with modeled microseism obtained from the reanalysis of
359 climate data, as done with WAVEWATCH III. Observations from a single seismometer correspond to
360 the sum of pressure sources originating from a radius of a few thousand kilometres around the station,
361 summing up along great circle paths and attenuating with distance. The observations have therefore a
362 very high temporal resolution while integrating spatially.

363 The analog seismic data was digitized to cover a 1-month interval centered on the tragic Big Flood
364 event that surged in the lowlands of the Netherlands, the United Kingdom and Belgium and it exhibits
365 changes in ground displacement amplitude and period. Those trends can be directly linked to the

366 behavior of specific sources in the North Atlantic Ocean, the Norwegian Sea, and the North Sea. While
367 trends in recovered and modeled microseism amplitude and period are similar, discrepancies between
368 the two data sets raise questions. For the Big Flood event itself, the failure of the model to accurately
369 reproduce the seismic energy recorded could be explained by a strong local source of primary microseism,
370 not modeled here, with wave periods around 7-8 s. This effect could also explain the 1-day difference in
371 the maximum of the energy observed for the 8-12 February storm. These results suggest the necessity
372 for additional research in order to provide a more precise combined model for primary and secondary
373 microseism activity. The 4-5 February event also exhibits differences between observed and modeled
374 data and such events are particularly interesting as they are the most difficult to accurately model due
375 to their remoteness from the shores and thus from most land-based observations. The uncertainties
376 on the instrument response could be a cause for differences between observed and modelled ground
377 motions, but our results suggest that different periods of activity exhibit different amplitudes while
378 sharing the dominant period, excluding at least partly an effect of the instrument. This should be
379 verified by adding more data (years) or more identical instruments (from other locations) and compare
380 with other instruments recording during the same time periods.

381 Our digitizing method is providing good results in the simple case of clear wiggles like the ones
382 recorded by the Galitzin seismometers. For more complex situations including overlaps, spikes, calibra-
383 tion pulses, etc. this method will fail. In that sense, solutions like the DigitSeis digitization software
384 (Bogiatzis and Ishii, 2016) are much more evolved and promising. Including computer vision and machine
385 learning for identifying the wiggles and their continuity could reduce the amount of human interaction
386 needed in the digitization process.

387 We show that the amplitude and dominant period of the ground motion displacement can be re-
388 constructed independently using vertical or horizontal seismometers. This will facilitate the use of even
389 earlier records, as horizontal seismographs were the first type of instruments installed worldwide. Analog
390 seismic data from different observatories can therefore be used to add constraints on atmosphere-ocean-
391 solid Earth couplings, to study different areas of the oceans and to better locate the microseismic sources,
392 similar to the recent studies with digital seismic data. Merging analog and digital data would facilitate

393 reanalyses over the entire 20th century.

394 Data & Resources

395 Analog seismograms used in this article are the property of the Royal Observatory of Belgium and can
396 be consulted at any time upon request to the ROB.

397 Scanned analog seismograms were processed using NumPy (Oliphant, 2006), SciPy (Jones et al.,
398 2001), Scikit-Image (van der Walt et al., 2014), ObsPy (Beyreuther et al., 2010; Krischer et al., 2015)
399 and Pandas (McKinney, 2012). Figures created with Matplotlib (Hunter, 2007) and maps were plotted
400 using Cartopy (Met Office, 2010). The modeled data from WAVEWATCH III are available from the
401 FTP server of Ifremer: <ftp://ftp.ifremer.fr/ifremer/ww3/HINDCAST/SISMO> (last accessed September
402 2019). It comes in NetCDF format (Rew and Davis, 1990) which are read using the NetCDF4-python
403 module (Whitaker et al., 2019). The whole processing has been implemented in Jupyter Notebooks
404 (Kluyver et al., 2016) and is accessible open and free on the authors' GitHub account ([https://github.](https://github.com/ThomasLecocq/SRL_2020_Historical)
405 [com/ThomasLecocq/SRL_2020_Historical](https://github.com/ThomasLecocq/SRL_2020_Historical), last accessed February 2020)

406 Acknowledgments

407 C. Hadziioannou is acknowledged for the discussions about the primary microseism in the North Sea.
408 C. Caudron, A. Watlet and K. Van Noten are acknowledged for the discussions and for proofreading of
409 the manuscript. Two anonymous reviewers and Dr Allison Bent, Editor in Chief, are acknowledged for
410 their comments and suggestions which improved the quality of the manuscript. This manuscript has
411 benefited greatly from Sharon K. Reamer's skilled copy-editing.

412 This article is the result of an idea that emerged from informal discussions at a summer school
413 organized as part of the COST-Action TIDES "Time Dependent Seismology" (COST-ES1401).

References

- 414
- 415 Albuquerque Seismological Laboratory (ASL)/USGS (1972). High-Gain Long-Period Network.
- 416 Albuquerque Seismological Laboratory (ASL)/USGS (1974). Seismic Research Observatory.
- 417 Albuquerque Seismological Laboratory (ASL)/USGS (1988). Global Seismograph Network (GSN -
418 IRIS/USGS).
- 419 Ardhuin, F., Stutzmann, E., Schimmel, M., and Mangeney, A. (2011). Ocean wave sources of seismic
420 noise. *Journal of Geophysical Research: Oceans*, 116(C9):C09004.
- 421 Aster, R. C., McNamara, D. E., and Bromirski, P. D. (2008). Multidecadal climate-induced variability
422 in microseisms. *Seismological Research Letters*, 79(2):194–202.
- 423 Aster, R. C., McNamara, D. E., and Bromirski, P. D. (2010). Global trends in extremal microseism
424 intensity. *Geophysical Research Letters*, 37(14).
- 425 Baskoutas, I. G., Kalogeras, I. S., Kourouzidis, M., and Panopoulou, G. (2000). A Modern Technique
426 for the Retrieval and Processing of Historical Seismograms in Greece. *Natural Hazards*, 21:55–64.
- 427 Becker, D., Kruse, T., Dethof, F., Weidle, C., and Hadziioannou, C. (2019). Microseism in the North
428 Sea: Tidal forcing, H/V-variability and a future monitoring network. *EGU General Assembly, Vienna,
429 Austria*, page 1.
- 430 Bernard, P. (1990). Historical sketch of microseisms from past to future. *Physics of the Earth and
431 Planetary Interiors*, 63(3-4):145–150.
- 432 Beyreuther, M., Barsch, R., Krischer, L., Megies, T., Behr, Y., and Wassermann, J. (2010). ObsPy: A
433 Python Toolbox for Seismology. *Seismological Research Letters*, 81(3):530–533.
- 434 Blackman, R. B. and Tukey, J. W. (1958). The measurement of power spectra from the point of view
435 of communications engineering - Part I. *Bell System Technical Journal*, 37(1):185–282.

- 436 Bogiatzis, P. and Ishii, M. (2016). DigitSeis: A New Digitization Software for Analog Seismograms.
437 *Seismological Research Letters*, 87(3):726–736.
- 438 Bromirski, P. D. and Chuang, S. (2003). SeisDig: Software to digitize scanned analog seismogram
439 images, user’s manual.
- 440 Camelbeeck, T. (1985). Some notes concerning the seismicity in Belgium. Magnitude scale. Detection
441 capability of the Belgian seismic stations. In *Seismic activity in western Europe*. P. Melchior, reidel
442 edition.
- 443 Choi, B. H., Kim, K. O., Yuk, J.-H., and Lee, H. S. (2018). Simulation of the 1953 storm surge in the
444 North Sea. *Ocean Dynamics*, 68(12):1759–1777.
- 445 Church, E. D., Bartlett, A. H., and Jourabchi, M. A. (2013). Raster-to-Vector Image Analysis for Fast
446 Digitization of Historic Seismograms. *Seismological Research Letters*, 84(3):489–494.
- 447 Dahm, T., Krüger, F., Essen, H.-H., and Hensch, M. (2005). Historic microseismic data and their
448 relation to the wave-climate in the North Atlantic. *Meteorologische Zeitschrift*, 14(6):771–779.
- 449 Darbyshire, J. (1954). Structure of microseismic waves: estimation of direction of approach by com-
450 parison of vertical and horizontal components. *Proceedings of the Royal Society of London. Series A,*
451 *Mathematical and Physical Sciences*, 223(1152):16.
- 452 Davis, G. K. (2007). History of the NOAA satellite program. *Journal of Applied Remote Sensing*,
453 1(1):012504.
- 454 Donn, W. L. and Blaik, M. (1952). A study and evaluation of the tripartite seismic method of locating
455 hurricanes. *Bulletin of the Seismological Society of America*, page 19.
- 456 Duda, R. O. and Hart, P. E. (1972). Use of the Hough transformation to detect lines and curves in
457 pictures. *Communications of the ACM*, 15(1):11–15.
- 458 Ebeling, C. W. (2012). Inferring Ocean Storm Characteristics from Ambient Seismic Noise. In *Advances*
459 *in Geophysics*, volume 53, pages 1–33. Elsevier.

- 460 El Bouch, A., Camelbeeck, T., and Martin, H. (2002). Atténuation des ondes sismiques en Belgique et
461 dans les régions limitrophes à partir de la coda des tremblements de terre locaux. *Geologica Belgica*,
462 5(1-2):17–29.
- 463 Friedrich, A., Krüger, F., and Klinge, K. (1998). Ocean-generated microseismic noise located with the
464 Gräfenberg array. *Journal of Seismology*, 2(1):47–64.
- 465 Galitzin, B. B. (1911). *Ueber ein neues aperiodisches horizontalpendel mit galvanometrischer fernreg-*
466 *istrierung*. Buchdr. der K. Akademie der wissenschaften.
- 467 Gerritsen, H. (2005). What happened in 1953? The Big Flood in the Netherlands in retrospect.
468 *Philosophical Transactions of the Royal Society of London A: Mathematical, Physical and Engineering*
469 *Sciences*, 363(1831):1271–1291.
- 470 Gilhousen, D. B. (1987). A Field Evaluation of NDBC Moored Buoy Winds. *Journal of Atmospheric*
471 *and Oceanic Technology*, 4(1):94–104.
- 472 Grevemeyer, I., Herber, R., and Essen, H.-H. (2000). Microseismological evidence for a changing wave
473 climate in the northeast Atlantic Ocean. *Nature*, 408(6810):349–352.
- 474 Gualtieri, L., Camargo, S. J., Pascale, S., Pons, F. M. E., and Ekström, G. (2018). The persistent
475 signature of tropical cyclones in ambient seismic noise. *Earth and Planetary Science Letters*, 484:287–
476 294.
- 477 Hanafin, J. A., Quilfen, Y., Ardhuin, F., Sienkiewicz, J., Queffeuilou, P., Obrebski, M., Chapron, B.,
478 Reul, N., Collard, F., Corman, D., and others (2012). Phenomenal sea states and swell from a North
479 Atlantic storm in February 2011: a comprehensive analysis. *Bulletin of the American Meteorological*
480 *Society*, 93(12):1825–1832.
- 481 Harjes, H. and Seidl, D. (1978). Digital recording and analysis of broad-band seismic data at Gräfenberg
482 (GRF) Array. *Journal Of Geophysics-Zeitschrift Fur Geophysik*, 44(5):511–523.
- 483 Hough, P. V. C. (1962). Method and means for recognizing complex patterns.

- 484 Hunter, J. (2007). Matplotlib: A 2d Graphics Environment. *Computing in Science Engineering*, 9(3):90–
485 95.
- 486 Jones, E., Oliphant, T., Peterson, P., et al. (2001). *SciPy: Open source scientific tools for Python*.
- 487 Juretzek, C. and Hadziioannou, C. (2016). Where do ocean microseisms come from? A study of Love-
488 to-Rayleigh wave ratios. *Journal of Geophysical Research: Solid Earth*, 121(9):6741–6756.
- 489 Juretzek, C. and Hadziioannou, C. (2017). Linking source region and ocean wave parameters with the
490 observed primary microseismic noise. *Geophysical Journal International*, 211(3):1640–1654.
- 491 Kluyver, T., Ragan-Kelley, B., Pérez, F., Granger, B., Bussonnier, M., Frederic, J., Kelley, K., Hamrick,
492 J., Grout, J., Corlay, S., Ivanov, P., Avila, D., Abdalla, S., and Willing, C. (2016). Jupyter Notebooks
493 - A publishing format for reproducible computational workflows. In Loizides, F. and Schmidt, B.,
494 editors, *Positioning and Power in Academic Publishing: Players, Agents and Agendas*, pages 87–90.
495 IOS Press.
- 496 Krischer, L., Megies, T., Barsch, R., Beyreuther, M., Lecocq, T., Caudron, C., and Wassermann, J.
497 (2015). ObsPy: a bridge for seismology into the scientific Python ecosystem. *Computational Science*
498 *& Discovery*, 8(1):014003.
- 499 Mayor, J., Traversa, P., Calvet, M., and Margerin, L. (2018). Tomography of crustal seismic attenuation
500 in Metropolitan France: implications for seismicity analysis. *Bulletin of Earthquake Engineering*,
501 16(6):2195–2210.
- 502 McComb, H. E. and Wenner, F. (1936). Shaking-table investigations of teleseismic seismometers. *Bul-*
503 *letin of the Seismological Society of America*, 26(4):26.
- 504 McKinney, W. (2012). *Python for data analysis: Data wrangling with Pandas, NumPy, and IPython*. ”
505 O’Reilly Media, Inc.”.
- 506 Meindl, E. A. and Hamilton, G. D. (1992). Programs of the national data buoy center. *Bulletin of the*
507 *American Meteorological Society*, 73(7):985–994.

- 508 Met Office (2010). *Cartopy: a cartographic python library with a matplotlib interface*. Exeter, Devon.
- 509 Ministère des Travaux Publics (1977). Plan Sigma pour la protection du bassin de l'Escaut Maritime
510 contre les marées-tempêtes de la mer du nord. Technical report, Ministère des Travaux Publics.
- 511 Nakata, N., Gualtieri, L., and Fichtner, A. (2019). *Seismic ambient noise*. Cambridge University Press.
- 512 Obrebski, M., Ardhuin, F., Stutzmann, E., and Schimmel, M. (2012). How moderate sea states can
513 generate loud seismic noise in the deep ocean. *Geophysical Research Letters*, 39(11).
- 514 Okal, E. A. (2015). Historical seismograms: Preserving an endangered species. *GeoResJ*, 6:53–64.
- 515 Oliphant, T. E. (2006). *Guide to NumPy*.
- 516 Otsu, N. (1979). A Threshold Selection Method from Gray-Level Histograms. *IEEE Transactions on*
517 *Systems, Man, and Cybernetics*, 9(1):62–66.
- 518 Pintore, S., Quintiliani, M., and Franceschi, D. (2005). Teseo: A vectoriser of historical seismograms.
519 *Computers & Geosciences*, 31(10):1277–1285.
- 520 Poli, P., Hersbach, H., Dee, D. P., Berrisford, P., Simmons, A. J., Vitart, F., Laloyaux, P., Tan, D. G.,
521 Peubey, C., Thépaut, J.-N., and others (2016). ERA-20c: An atmospheric reanalysis of the twentieth
522 century. *Journal of Climate*, 29(11):4083–4097.
- 523 Rascle, N. and Ardhuin, F. (2013). A global wave parameter database for geophysical applications. Part
524 2: Model validation with improved source term parameterization. *Ocean Modelling*, 70:174–188.
- 525 Reguero, B. G., Losada, I. J., and Méndez, F. J. (2019). A recent increase in global wave power as a
526 consequence of oceanic warming. *Nature communications*, 10.
- 527 Rew, R. and Davis, G. (1990). NetCDF: an interface for scientific data access. *IEEE computer graphics*
528 *and applications*, 10(4):76–82.
- 529 Roux, P., Bindi, D., Boxberger, T., Colombi, A., Cotton, F., Douste-Bacque, I., Garambois, S., Gueguen,
530 P., Hillers, G., Hollis, D., Lecocq, T., and Pondaven, I. (2018). Toward Seismic Metamaterials: The
531 METAFORÉT Project. *Seismological Research Letters*, 89(2A):582–593.

- 532 Royal Observatory of Belgium (1985). Belgian Seismic Network.
- 533 Shearer, P. M. (2019). *Introduction to seismology*. Cambridge university press.
- 534 Somville, O. (1914). Observations sismologiques faites à Uccle, en 1910, 1911, 1912 et 1913. Technical
535 report, Royal Observatory of Belgium.
- 536 Somville, O. (1922a). Constantes des sismographes galitzine. In *Annales de l'Observatoire Royal de*
537 *Belgique*, volume 1.
- 538 Somville, O. (1922b). Sur la methode d'enregistrement galvanometrique appliquee aux sismographes
539 galitzine. In *Annales de l'Observatoire Royal de Belgique*, volume 1.
- 540 Somville, O. (1930). Bulletin Séismique de l'Observatoire royal de Belgique. Technical report, Royal
541 Observatory of Belgium.
- 542 Somville, O. (1931). Bulletin Séismique de l'Observatoire royal de Belgique. Technical report, Royal
543 Observatory of Belgium.
- 544 Somville, O. (1932). Bulletin Séismique de l'Observatoire royal de Belgique. Technical report, Royal
545 Observatory of Belgium.
- 546 Somville, O. (1933). Bulletin Séismique de l'Observatoire royal de Belgique. Technical report, Royal
547 Observatory of Belgium.
- 548 Somville, O. (1934). Bulletin Séismique de l'Observatoire royal de Belgique. Technical report, Royal
549 Observatory of Belgium.
- 550 Somville, O. (1935). Bulletin Séismique de l'Observatoire royal de Belgique. Technical report, Royal
551 Observatory of Belgium.
- 552 Somville, O. (1936). Bulletin Séismique de l'Observatoire royal de Belgique. Technical report, Royal
553 Observatory of Belgium.
- 554 Somville, O. (1937a). Bulletin Séismique de l'Observatoire royal de Belgique. Technical report, Royal
555 Observatory of Belgium.

- 556 Somville, O. (1937b). Un nouveau type de séismographe vertical. *Publications du Bureau central*
557 *séismologique international*, Fascicule 15:137–145.
- 558 Somville, O. (1953). Bulletin Séismique de l’Observatoire royal de Belgique. Technical report, Royal
559 Observatory of Belgium.
- 560 Stopa, J. E., Arduin, F., Stutzmann, E., and Lecocq, T. (2019). Sea State Trends and Variability: Con-
561 sistency Between Models, Altimeters, Buoys, and Seismic Data (1979–2016). *Journal of Geophysical*
562 *Research: Oceans*, 124(6):3923–3940.
- 563 Stutzmann, E., Arduin, F., Schimmel, M., Mangeney, A., and Patau, G. (2012). Modelling long-term
564 seismic noise in various environments. *Geophysical Journal International*, 191(2):707–722.
- 565 Tolman, H. L. and the WAVEWATCH III Development Group (2014). User Manual and system docu-
566 mentation of WAVEWATCH III version 4.18. Technical Note 316, NOAA/NWS/NCEP/MMAB.
- 567 Van Camp, M. and Camelbeeck, T. (2004). Histoire des stations sismiques belges: de la station
568 «Solvay» au réseau national de surveillance sismique. *Ciel et Terre*, 120(6):162–176.
- 569 van der Walt, S., Schönberger, J. L., Nunez-Iglesias, J., Boulogne, F., Warner, J. D., Yager, N., Gouillart,
570 E., and Yu, T. (2014). scikit-image: image processing in Python. *PeerJ*, 2:e453.
- 571 Van Noten, K., Lecocq, T., Sira, C., Hinzen, K.-G., and Camelbeeck, T. (2017). Path and site effects
572 deduced from transfrontier internet macroseismic data of two recent M4 earthquakes in NW Europe.
573 *Solid Earth Discussions*, pages 1–33.
- 574 Wadey, M. P., Haigh, I. D., Nicholls, R. J., Brown, J. M., Horsburgh, K., Carroll, B., Gallop, S. L.,
575 Mason, T., and Bradshaw, E. (2015). A comparison of the 31 January–1 February 1953 and 5–6
576 December 2013 coastal flood events around the UK. *Frontiers in Marine Science*, 2.
- 577 Wang, M., Jiang, Q., and Pan, Z. (2014). A New Curve Tracing Algorithm Based on Local Feature in
578 the Vectorization of Paper Seismograms. *Sensors & Transducers*, 165(2):4.

- 579 Welch, P. (1967). The use of fast Fourier transform for the estimation of power spectra: A method
580 based on time averaging over short, modified periodograms. *IEEE Transactions on Audio and Elec-*
581 *troacoustics*, 15(2):70–73.
- 582 Wemelsfelder, P. J. (1953). The disaster in The Netherlands caused by the storm flood of February 1,
583 1953. *Coastal Engineering Proceedings*, 1(4):18.
- 584 Wenner, F. and McComb, H. E. (1936). The Galitzin seismometer: Discrepancies between the Galitzin
585 theory and the performance of a Wilip-Galitzin seismometer. *Bulletin of the Seismological Society of*
586 *America*, 26(4):317–322.
- 587 Whitaker, J., Khrulev, C., Huard, D., Paulik, C., Stephan Hoyer, Filipe, Pastewka, L., Mohr, A.,
588 Marquardt, C., Couwenberg, B., Whitaker, J., Cuntz, M., Bohnet, M., Brett, M., Hetland, R.,
589 Korenčiak, M., barronh, Onu, K., Helmus, J. J., Hamman, J., Barna, A., fredrik 1, Koziol, B.,
590 Kluyver, T., May, R., Smrekar, J., Barker, C., Silva, D. d., Gohlke, C., and Kinoshita, B. P. (2019).
591 Unidata/netcdf4-python: version 1.5.1.2 release.
- 592 Wolf, J. and Flather, R. A. (2005). Modelling waves and surges during the 1953 storm. *Philosophical*
593 *Transactions of the Royal Society of London A: Mathematical, Physical and Engineering Sciences*,
594 363(1831):1359–1375.

595 Authors' full mailing address

- 596 • Thomas Lecocq, Fabienne Collin & Thierry Camelbeeck: Royal Observatory of Belgium, Seismology-
597 Gravimetry, Avenue circulaire 3, 1180 Uccle, Belgium
- 598 • Fabrice Ardhuin: Univ. Brest, CNRS, IRD, Ifremer, Laboratoire d'Océanographie Physique et
599 Spatiale (LOPS), IUEM, 29280, Brest, France.

600 Tables

Table 1: 1953 parameters for the Galitzin seismometers at ROB (Somville, 1953), where T is the period of the pendulum, T_1 the period of the galvanometer, l the reduced pendulum length, μ the damping constant, A_1 the distance of the drum from the galvanometer mirror and k the transfer factor (Galitzin, 1911, p. 103). The two values for k for the vertical instrument are 290 from the bulletin (Somville, 1953) and the newly determined value, 97, based on the data (see text).

Instrument	T (s)	T_1 (s)	l (mm)	μ	A_1 (mm)	k
Galitzin E-W	21.5	21.8	123.8	+0.2	1040	38
Galitzin N-S	24.5	21.8	124.7	+0.2	1040	38
G.-Willip-Somville V	10.0	10.15	173.8	0.0	1060	290 (97)

601 List of Figures

- 602 1 The amplitude response of the Galitzin seismometers owned by the ROB (Somville, 1930,
603 1937a, 1953) 28
- 604 2 Map of the 1953 storm path 72 hours before until 24 after the Big Flood with the atmo-
605 spheric pressure and wind fields 6 hours before the Big Flood, redrawn from Wadey et al.
606 (2015). The dashed ellipses indicate the region where dramatic flooding occurred (red)
607 and the area of maximal sensitivity (black, based on Ardhuin et al. (2011)) for the UCC
608 seismic station (black star). 29

- 609 3 15 January-15 February 1953 displacement power spectral density (PSD) spectrograms
 610 based on the automatically extracted time series for the Vertical, East-West and North-
 611 South components, and below, the result of the modeling using WAVEWATCH III and
 612 coastal reflections (REF102040). The thin white contours that highlight the -130 and
 613 -120 dB levels are indicated for illustration purposes only. The thick dashed white line
 614 indicates the time of occurrence of the Big Flood. The arrows indicate the five periods
 615 of significant microseismic activity, labelled E1 to E5 in the text and the following figures. 30
- 616 4 Modeled daily average microseismic sources obtained from Ocean Modeling: the power
 617 spectral density of equivalent surface pressure summed over all periods, not corrected for
 618 coupling (WAVEWATCH III and coastal reflections REF102040). The arrows indicate
 619 the five periods of significant microseismic activity. The map extents are east-west: -40,
 620 15 degrees, north-south: 35, 75 degrees. The map projection Lambert Conform (central
 621 latitude and longitude: 50.0 and 0.0 degrees.) 31
- 622 5 Comparison of the ground displacement amplitude (above) and its dominant period (be-
 623 low) for the modeled and observed data from digitized seismograms of the UCC station.
 624 Two ocean generated ground motion models with different Q factor are presented. The
 625 arrows indicate the five periods of significant microseismic activity seemingly higher than
 626 a background level that could be estimated at $0.25 \mu m$: 17-21 January, 26-30 January,
 627 31 January - 2 February, 4-5 February and finally 8-12 February. 32

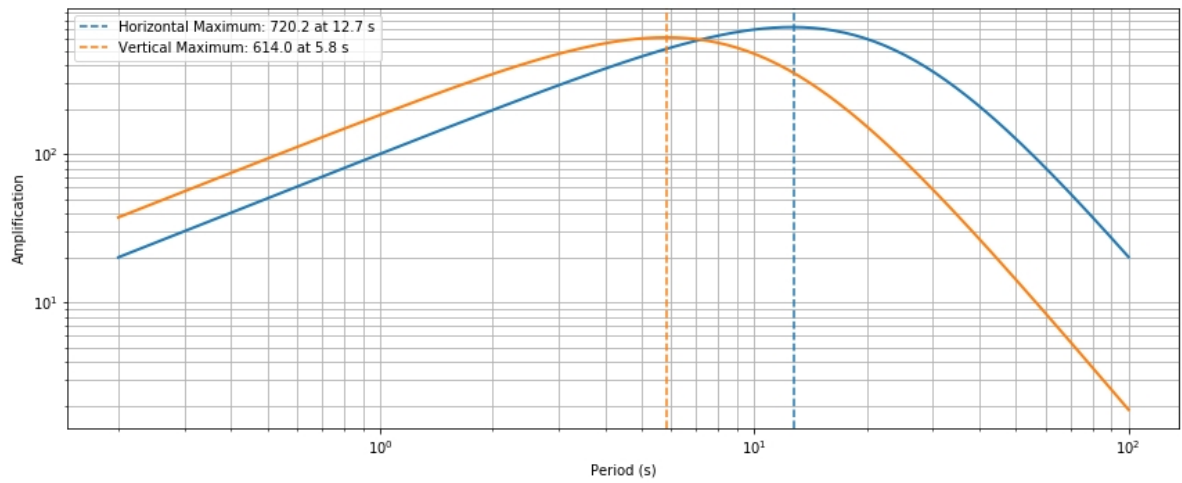


Figure 1: The amplitude response of the Galitzin seismometers owned by the ROB (Somville, 1930, 1937a, 1953)

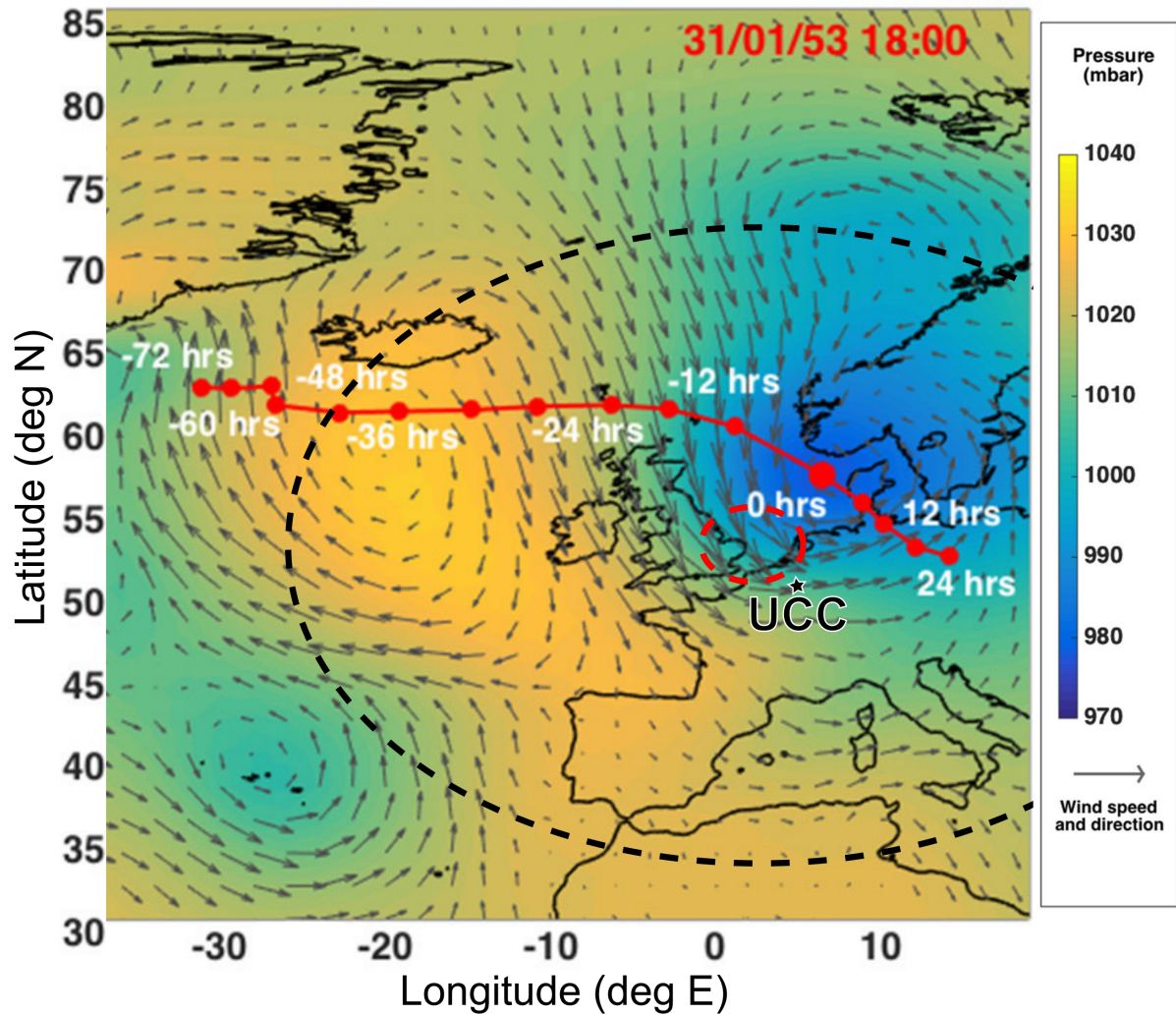


Figure 2: Map of the 1953 storm path 72 hours before until 24 after the Big Flood with the atmospheric pressure and wind fields 6 hours before the Big Flood, redrawn from Wadey et al. (2015). The dashed ellipses indicate the region where dramatic flooding occurred (red) and the area of maximal sensitivity (black, based on Arduin et al. (2011)) for the UCC seismic station (black star).

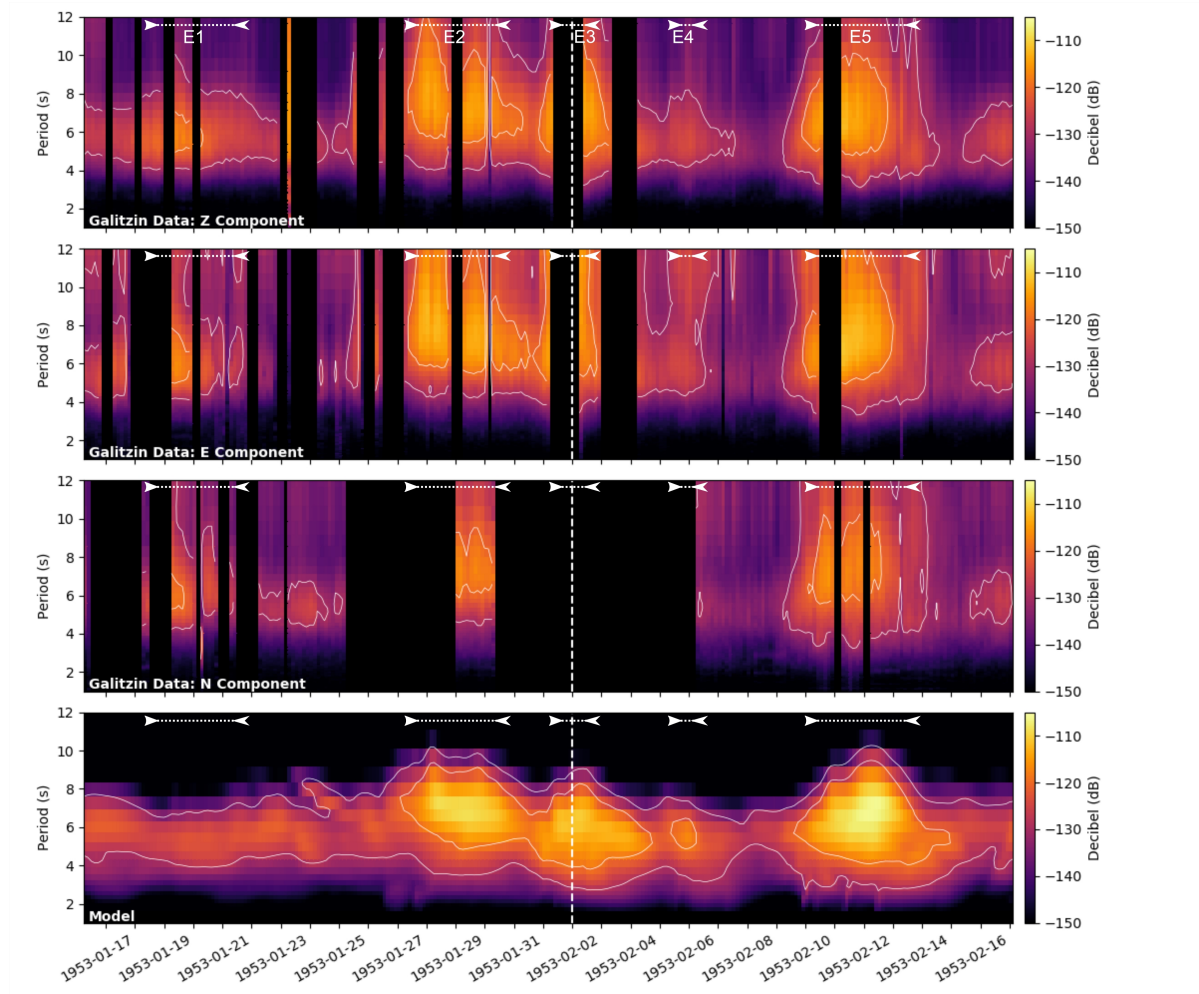
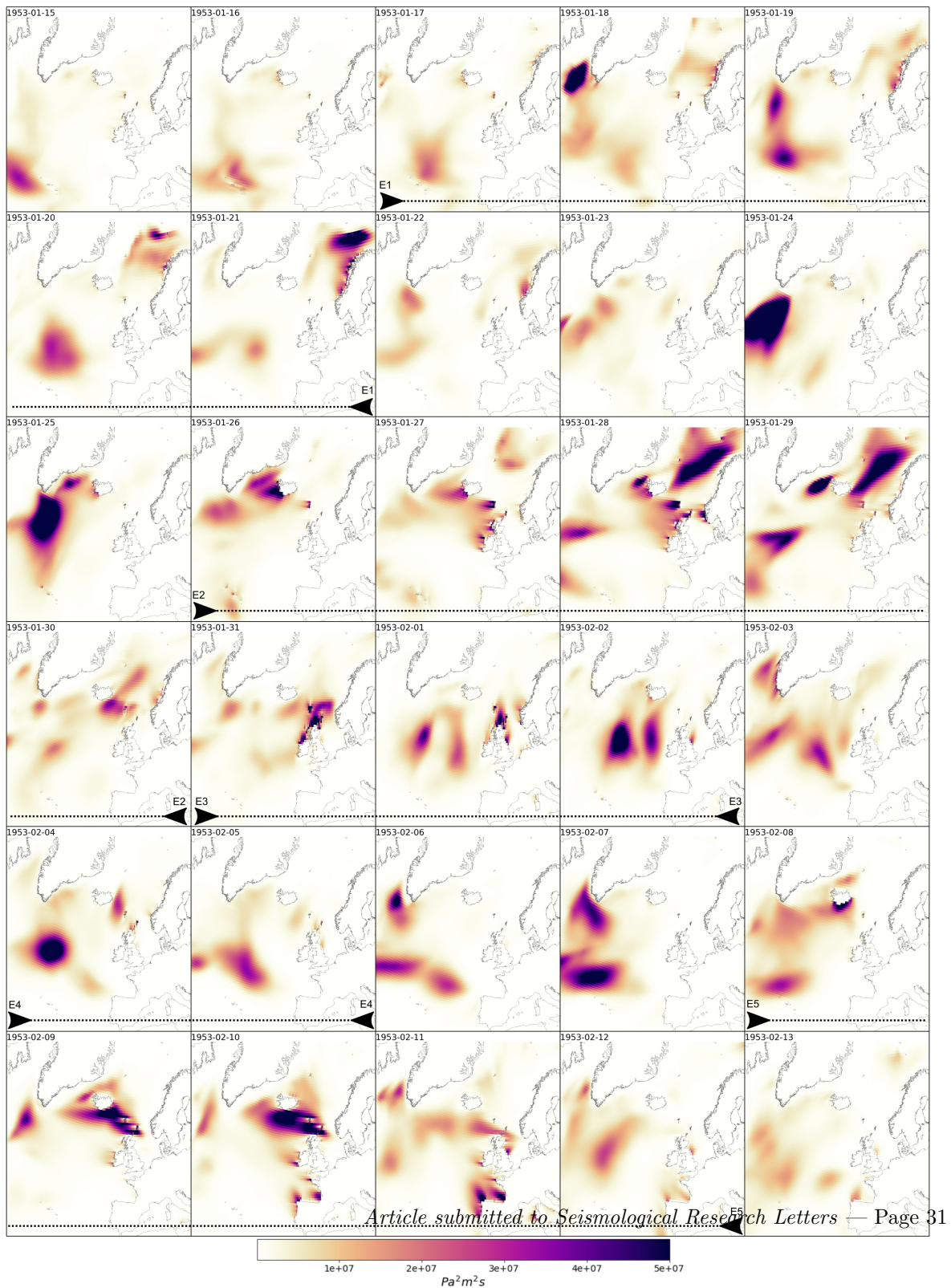


Figure 3: 15 January-15 February 1953 displacement power spectral density (PSD) spectrograms based on the automatically extracted time series for the Vertical, East-West and North-South components, and below, the result of the modeling using WAVEWATCH III and coastal reflections (REF102040). The thin white contours that highlight the -130 and -120 dB levels are indicated for illustration purposes only. The thick dashed white line indicates the time of occurrence of the Big Flood. The arrows indicate the five periods of significant microseismic activity, labelled E1 to E5 in the text and the following figures.



Article submitted to *Seismological Research Letters* — Page 31

Figure 4: Modeled daily average microseismic sources obtained from Ocean Modeling: the power spectral density of equivalent surface pressure summed over all periods, not corrected for coupling (WAVEWATCH III and coastal reflections REF102040). The arrows indicate the five periods of significant microseismic activity. The map extents are east-west: -40. 15 degrees, north-south: 35. 75 degrees. The

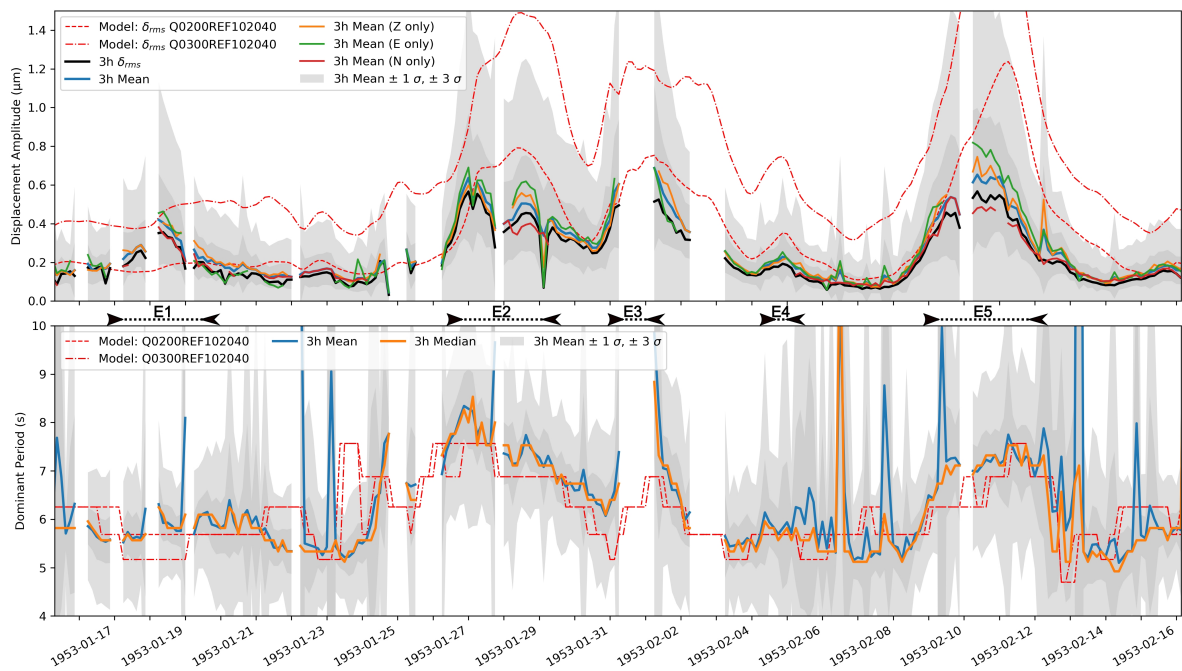


Figure 5: Comparison of the ground displacement amplitude (above) and its dominant period (below) for the modeled and observed data from digitized seismograms of the UCC station. Two ocean generated ground motion models with different Q factor are presented. The arrows indicate the five periods of significant microseismic activity seemingly higher than a background level that could be estimated at $0.25 \mu\text{m}$: 17-21 January, 26-30 January, 31 January - 2 February, 4-5 February and finally 8-12 February.